Published in final edited form as:
Microcirculation. 2012 October ; 19(7): 652–663. doi:10.1111/j.1549-8719.2012.00200.x.

Skin Graft Vascular Maturation and Remodeling: A Multifractal Approach to Morphological Quantification

Daniel J. Gould, PhD[1,2] and **Gregory P. Reece, MD**[2]

[1]Medical Scientist Training Program (MD/PhD), Baylor College of Medicine, Houston, Texas

[2]Department of Plastic Surgery, The University of Texas MD Anderson Cancer Center, Houston, Texas

Abstract

Objective—One important contributor to tissue graft viability is angiogenic maturation of the graft tissue bed. This study uses scale-invariant microvascular morphological quantification to track vessel maturation and remodeling in a split-thickness skin grafting model over 21 days, comparing the results to classical techniques.

Methods—Images from a previous study of split-thickness skin grafting in rats were analyzed. Microvascular morphology (fractal and multifractal dimensions, lacunarity, and vessel density) within fibrin interfaces of samples over time was quantified using classical semi-automated methods and automated multifractal and lacunarity analyses.

Results—Microvessel morphology increased in density and complexity, from 3 to 7 days after engraftment and then regressed by 21 days. Vessel density increased from 0.07 on day 3 to 0.20 on day 7 and then decreased to 0.06 on day 21. A similar trend was seen for the fractal dimension which increased from 1.56 at 3 days to 1.77 at 7 days then decreased to 1.57 by 21 days. Vessel diameters did not change while complexity and density did, signaling remodeling.

Conclusions—This new automated analysis identified design parameters for tissue engraftment and could be used in other models of graft vessel biology to track proliferation and pruning of complex vessel beds.

Keywords

Microcirculation; Split Thickness Skin Graft; Microvascular Morphology; Multifractal Analysis

Introduction

Grafting is a common medical procedure wherein tissues from one site on the patient are transplanted to a recipient site that requires supplementation (1). Skin is one of the most frequently transplanted tissues in grafting procedures and is commonly used to cover defects resulting from trauma, burns, infection, and diseases of the microvasculature (2). Skin-grafting strategies include the use of split-thickness and full-thickness skin grafts, allograft materials like decellularized human cadaver skin, and acellular synthetic scaffolds (3,4). Although skin grafting is a very common surgical procedure, little is known about the microcirculation and microvascular morphology during skin graft maturation and remodeling. The early stages of a skin graft mimic the host wound response: there is an initial release of angiogenic signals and growth factors and then eventual angiogenesis and

Corresponding Author: Daniel J. Gould, PhD., One Baylor Plaza, Houston Texas, 77030, djgould@bcm.edu; dr.danjgould@gmail.com, Tel: 916-806-9649.

perfusion of the graft followed by the remodeling and pruning of unnecessary vessels (5). The process of vessel growth, anastamosis, and remodeling is complex, and knowledge of the microvessel morphology at different stages in the process may aid in the design of synthetic engineered scaffolds for the repair of tissues, including skin.

In previous studies, our laboratory developed a rat model of autologous skin grafting in which the rat is first de-epithelialized over a small region of the flank and then a split-thickness graft is harvested from the future implantation site to cover the defect (6). This method has been used to closely examine the developing microvasculature in the wound bed and graft. In fact, using this model, our laboratory has been able to precisely describe several quantitative parameters of vessel morphology in the fibrin interface between the graft and the recipient site (7). These studies have laid the groundwork for investigations aimed at even greater quantification of the microvascular structures in split thickness skin grafts. Recently, several new tools have been developed for use in quantifying vessel morphology, including fractal dimension, lacunarity, and multifractal analysis (8). In short, box-counting algorithms are used to quantify the fractal dimension (9) and can be extended to quantify the multifractal spectrum of images of sample vessels. These morphological parameters provide detailed space-filling information about the vascular beds (10–12). The concept of fractals was first described by Mandelbrot in 1967 in his seminal paper describing a method for measuring the coastline of Great Britain (13). He made the argument that the length of the coastline was dependent on the length of the ruler used to measure it. Thus, by plotting the relationship between the length of the ruler used and the measured length of the coastline, he found a logarithmic value that could be used to predict measured length on the basis of ruler size. Using the slope of the transformed log plot and comparing it to similar measurements of other coastlines or objects, he found that more complex objects (with rougher or “irregular” surfaces) had steeper curves, similar to those seen with smaller rulers, which resulted in greater measured length. Thus, the slope of the log-log relation gave a surrogate measure of complexity or roughness and allowed for new comparisons to be made. The measured slope was referred to as a fractal dimension, as it was a dimensional measure of complexity but a non-Euclidean geometrical value.

Mandelbrot continued to interrogate the complexity of space surrounding objects, developing the lacunarity parameter (to look at the lacunae or ‘lakes’ of emptiness that surround an object), which can be measured with a similar gliding box algorithm (14). This parameter has been used by others to investigate nonvascular space around vessel beds (presumably metabolic tissue); thus, in combination with the fractal dimension, it helps to quantify the complexity of vessel beds and their surrounding tissues (8,14). These tools for measuring complexity are incredibly valuable because they provide scale-invariant measures of object morphology, and they have been widely applied in soil science (15), geography (10), and biological sciences (16,17).

These tools for measuring complexity are well suited for use in assessing vessel morphology, and as Mandelbrot initially postulated, they can relate the complexity of vessel beds and their surrounding tissues to each other under differing developmental (8), physiologic (12,18,19), pathologic (20,21), or experimental states (22,23). Scale-invariant parameters provide information about the way the vessels fill the space that is independent of the scale used to examine them. Furthermore, the analysis of conventional skin grafting using these parameters will provide useful, scale-invariant information about the complexity of vessel distribution in tissues and inform the design and development of a tissue-engineered substitute. This information may also be critical for the delivery of oxygen and metabolites at appropriate levels to the desired tissues, as structure and function are usually found to be intertwined. In this study, we re-examined the data initially presented by Wu and colleagues (7) in order to apply this novel quantification system to the images of vessels in

the fibrin interface between graft and host tissues. Our findings show that this new method provides more insight into the remodeling events that occur early and late in the development and pruning of blood vessels and shape the network complexity associated with the skin grafts.

Materials and Methods

Graft Implantation

In this study, we used images of tissue samples previously collected and presented by Wu and colleagues and the graft implantation and sample preparation were previously described in that study (7). Briefly, animal surgeries were performed in laboratory space accredited by the Association for Assessment and Accreditation of Laboratory Animal Care. Sprague-Dawley rats were matched for age and weight and then randomized to one of five groups, each containing three animals.

The rats were anesthetized using an intramuscular injection of ketamine (64 mg/ml), xylazine (3.6 mg/ml), and atropine (0.07 mg/ml), along with perioperative isoflurane (0.2%), as needed. The animals' backs and flanks were shaved and then a depilatory agent was applied to remove all hair. A 1.5-cm-diameter circular graft was cut with an electric dermatome set to 0.3 mm to create the split-thickness graft. The graft was then cut into 1-by-1-cm squares using a template and stored on a saline-moistened sponge until needed. The site where the skin graft was harvested on the back of the rat was excised to remove the dermis and panniculus carnosis, which left a defect approximately the same diameter as the graft. After the skin edge of the defect was sutured to the underlying muscle, the grafts were implanted on the exposed latissimus muscle. The rats were euthanized by CO_2 asphyxiation on postoperative days (POD) 3, 7, 10, 14, or 21. The graft and underlying muscle were removed, flash frozen, and serially sectioned for immunohistochemical and imaging analysis. The frozen tissue was sectioned 8 um thick to preserve the three-dimensional architecture of the microvasculature. For each graft the imaged area for comparison was 444 microns by 444 microns, which after imaging became a 512 by 512 pixel image. The blood vessels were stained with anti-rat CD 31 monoclonal antibodies (Serotec, Raleigh, NC), and then the tissues were imaged using a 20× objective on an Olympus ix-70 inverted bright field microscope (Olympus, Mellville, NY) with a color CCD camera (RT SPOT Diagnostic Instruments, Sterling Heights, MI).

Image Analysis

Images of the CD 31-(also referred to as PECAM) stained microvasculature were collected in succession and tiled, and the threshold for the signal intensity of the stained tissue in each section was set as previously described (7). To standardize the analysis, 80-micron-thick segments, which included ten successive images of the same tissue, were used from all samples (see figure 1A).

The 80-micron-thick stacks of thresholded images were first compressed into projection images using ImageJ software (z-projection program; National Institutes of Health) (24). Next, the projected binary images were input into a special program designed with MATLAB software (Natick, MA) to overlay the images with boxes of different pixel sizes (1×1, 2×2, 4×4, 16×16…512×512). The number of boxes required to cover the images at each box size was then calculated. This algorithm is available free online at MATLAB central in several forms,(9,25,26) two were developed by Gould and Vadakkan and were previously described in publication (8).

Fractal Analysis, Vessel Density, Multifractal Analysis and Lacunarity

The fractal and multifractal dimensions, lacunarity, and vessel density of the projection images were analyzed for all samples. Algorithms written to determine these values were previously published (8) and a detailed description of the methodology behind these techniques and the algorithms can be found there. The reported values are the average values of the measured parameters for all of the animals examined in each experimental group. These averages were calculated from measurements from at least three tissue samples from each animal and from at least three animals from each time point for all five time points. They were then compared to the numbers of vessels, area fractions, and vessel diameters at the time points of 3, 7, and 10 days from the Wu and colleagues' study (7).

Projection images of the developing vessels in the fibrin interface were analyzed using several algorithms that are available free online (8,9,14,25). These algorithms were run in parallel using MATLAB software (Mathworks, Natick, MA), and the output data were then analyzed by comparison of the means using analysis of variance tests with post hoc Tukey least-significant-difference analysis.

The box counting algorithm, designed to determine the fractal dimension and the generalized fractal dimensions for the multifractal analysis, functions in this way. First, a processed binary image of vessels is obtained and converted to a matrix where pixels are represented by a value of 1 (positive staining signal) or zero (no signal). The representative image is then overlaid with a grid, which creates evenly spaced boxes with side length ε (see figure 2). Each box is a perfect square, and the lengths are all scaled multiples of 2. Each box with at least one positive pixel is counted, and the total number of boxes with at least one positive pixel, or $N(\varepsilon)$, is recorded. Next, the total number of positive boxes, $N(\varepsilon)$, is plotted against the length of the boxes, ε. This relationship takes a logarithmic form when plotted, and then the plot is transformed to a log-log plot, which appears as a linear relationship. The slope of this linear plot is equivalent to the fractal dimension, D0. Thus, D0 relates the number of positive boxes to the size of the box on many different scales.

This approach may be extended to determine the relationship between other parameters associated with the boxes. On a given scale represented by ε, boxes can have similar densities and, thus, may have differing correlation values at different functions (or box sizes); this can be measured and is given by the value D1, or the correlation dimension. Also, as the scale changes, the amount of information contained in the box can change, so that as the box size approaches one pixel, less and less information can be stored in the system (one pixel boxes can only have the value of 1 or zero). Thus, the change in entropy over scale can also be plotted, and the dimension D2 represents the relationship between scale and information stored in the unit of scale and is known as the entropy dimension.

The relationships among these three moments (D0, D1, and D2) are examined in the multifractal analysis, which compares the relative complexity of the area of the vessels (fractal dimension or capacity dimension, D0), the complexity of the distribution of the vessels (correlation dimension, D1), and the complexity of the information contained within the system (entropy dimension, D2).

The complete generalized dimensions (D0, D1, D2) can be measured and plotted using a Legendre transformation to form the multifractal spectra, which can then be used to statistically separate groups of images (15). To measure the generalized fractal dimensions of a binary image, the binary image is overlaid with $N(\varepsilon)$ boxes, each of width ε. Associated with each box of index i is a measure $P_i(\varepsilon)$, which is defined as the number of signal pixels in the i^{th} box of width ε divided by the total number of signal pixels in the image (pixel density). The q^{th} moment of $P_i(\varepsilon)$ is given by the equation stated below.

$$\mu_i(q,\varepsilon)=[P_i(\varepsilon)]^q/\sum_i[P_i(\varepsilon)]^q \quad (1)$$

$\mu_i(q,\varepsilon) \in [0,1]$ for each value of q. In this case, we used q ranges from −2 to +2 in steps of 0.1.

Also, $\sum_i [P_i(\varepsilon)]^q \sim \varepsilon^{\tau(q)}$.

The functions of the moments f(q) and α(q) are defined using the following two equations:

$$f(q)=\lim(\varepsilon \to 0)[\{\sum_i \mu_i(q,\varepsilon)\log(\mu_i(q,\varepsilon)\}/\log\varepsilon] \quad (2)$$

$$\alpha(q)=\lim(\varepsilon \to 0)[\{\sum_i \mu_i(q,\varepsilon)\log(P_i,(\varepsilon))\}/\log\varepsilon] \quad (3)$$

The multifractal spectrum is the f (α) - α curve defined by the equation f (α) = αq − τ(q).

Generalized fractal dimensions are defined through the scaling relation $\sum_i [P_i(\varepsilon)]^q \sim \varepsilon^{\tau(q)}$, where $\tau(q) = (q-1) D_q$, $q \in (-\alpha, +\alpha)$, and $i \in [1, N(\varepsilon)]$ (15). Also $\mu_i(q,\varepsilon) = [P_i(\varepsilon)]^q / \sum_i [P_i(\varepsilon)]^q$ where $i \in [1, N(\varepsilon)]$ (15). In the case of simple fractals (monofractal structures), D_q proves independent of the value of q and $D_0 = D_1 = D_2$.. In the case of a multifractal structure, D_0, D_1, and D_2 are related by the inequality $D_0 \geq D_1 \geq D_2$.. A structure is only considered multifractal if there is a difference between D_0, D_1, and D_2.

Plotting Multifractal Spectra

A description of the generalized fractal dimensions in a manner analogous to the box counting dimension is made by changing the variables from (q, τ) to (α, f) such that $\alpha = \partial\tau / \partial q$ and f (α) = αq − τ. This transformation is called a Legendre transformation (28,29) and has been used before to relate the D(q) spectrum to the f(α) spectrum (12). The number of boxes N(α) for which the probability $P_i(\varepsilon)$ has exponents between α and α + dα scales as $\varepsilon^{-f(\alpha)}$. Thus, f(α) is the fractal dimension of the set of boxes for which the exponent is α. The plot of f(α) against α(q) is referred to as the multifractal spectrum in this and other papers (12,15), and the comparison of these spectra has previously been demonstrated by Chhabra and Jensen (30). To calculate f(α), two functions f(q) and α(q) should be calculated. The functions f(q) and α(q) are defined through equations 2 and 3. f(q) is the slope of the line obtained by plotting ($\sum_i \mu_i(q,\varepsilon) \log(\mu_i(q,\varepsilon))$) against log ε, and α(q) is the slope of the line obtained by plotting ($\sum_i \mu_i(q,\varepsilon) \log(P_i(\varepsilon))$) against log ε. f(q) and α(q) are functions of the moments of the distribution P_i. The values of these functions for each order of the moment q allow us to construct the multifractal spectrum.

In simplified terms, to extend the simple fractal quantification to a multifractal method, at each size a box can be determined positive, but it also may have a measureable density of positive pixels. For instance, several of the boxes in figure 2 range from 10% full to 60% full. The equation to determine the generalized dimension, d(q) is shown. The value to be determined is d(q) where q can be any value, but particular interest has been on q=1 and q=2. Q=1 is the entropy (or information) dimension and captures the density of pixels at each box size, so that as the box size decreases, the total information decreases and becomes homogenous. Q=2 is the correlation dimension which takes into account two boxes at once, if boxes are the same they exhibit maximum overlap, if they differ, there is a decay function associated, and this decay can be plotted (representing a power function with a measureable slope). This encapsulates the concept that multifractals contain fractal behavior in different

scales and dimensions. To determine the values of D1 and D2 for discrete values of q and ε, the following equation can be utilized.

$$D_q=\lim_{(\varepsilon->0)}[1/1-q]^*[\log\left\{\sum_j[(\mu(C_j))]^q\right\}/\ell n(1/\varepsilon)] \quad (4)$$

Symmetry and Heterogeneity Analysis

The multifractal spectra output values can be studied to provide information about the symmetry and heterogeneity of the spectral curves. Using the plot of $\alpha(0)$ versus D_0 for the split thickness skin grafts at different time points the magnitude of the difference in the values of $\alpha(0)$ and D_0 can serve as a measure of heterogeneity of the vascular pattern. This is then defined as the range of scaling exponents required to characterize the pattern. One feature of multifractal behavior is the heterogeneity of the scaling behavior of the vascular pattern or different regions within. The plot of $\alpha(0)$ and D_0, allows the direct assessment of the multifractal behavior of the vascular bed, in that if the data points lie on a 1:1 line, the pattern is not heterogeneous, and therefore it can be characterized by the simple fractal dimension, D_0 alone.

Symmetry analysis of the multifractal spectral output yields information about the distribution of the fractal dimensions of the vessel pattern (represented by the space occupied by vessels in the image). Symmetry of a multifractal spectrum is determined through the measurement of the widths $(\alpha(q_{i,-}) - \alpha(0))$ and $(\alpha(0) - \alpha(q_{i,+}))$ (15). $q_{i,-}$ and $q_{i,+}$ correspond to the negative and positive values of q from the range of q values in which multifractal scaling is present, determined from analysis of the R^2 values for each value of alpha, where the R^2 values are above 95% representing a close fit to logarithmic behavior. A spectrum is determined to be symmetric if the two widths are equal. Perturbations in the symmetrical distribution of the multifractal spectra highlight differences in the contribution of the network and the surrounding emptiness (which is actually supportive non endothelial tissue as well). These steps in the analysis are critical to understanding the actual meaning behind the spectra in any multifractal analysis and have previously been developed for analysis by Posadas et al. (15).

Lacunarity

The lacunarity is defined (when a box size is ε) as $L(\varepsilon) = (N(\varepsilon) \times Q_2) / Q_1^2$. $Q_1 = \sum_i p(i,\varepsilon)$; the sum of the square of the number of signal pixels in each box $Q_2 = \sum_i p(i,\varepsilon)^2$. In the split thickness skin graft vascular networks analyzed in this study the lacunarity function $L(\varepsilon)$ resembled a hyperbolic curve. With this observation, the lacunarity function was fitted with the hyperbolic function, $L(\varepsilon) = b / \varepsilon^a + c$ (31) where b (referred to as the lacunarity parameter) is related to the concavity of the hyperbola (as previously demonstrated by Zaia et al. (31)). Note that when the values for b are low, this defines hyperbolic curves with wide concavity (high lacunarity). This implies that low b values describe objects with a large distribution of non-vascular gaps throughout, or high levels of “gappiness” or lacunarity, which in this study represents non endothelial or non-vascular tissues in the grafts.

For fractal patterns, lacunarity plots demonstrate linear behavior on log-log graphs. Taking the logarithm of the hyperbolic function $L(\varepsilon) = b/\varepsilon^a + c$ we get $\ln(L(\varepsilon)-c) = \ln(b) - a \ln(\varepsilon)$ which is the equation of a straight line. This along with the R^2 values obtained from the fitting of the function to the data points justifies the use of the hyperbolic function.

Results

Projection images from the tissues at the different time points showed clear signs of vascular remodeling (see figure 1 B), as evidenced by a relatively low density of vessels at POD 3, followed by a large growth of vessels by POD 7, and then vessel pruning up to POD 21. Analyses of the vessel density, fractal dimension, generalized fractal dimensions (from the multifractal analysis), and lacunarity were performed on the images using the automated algorithms. The output dataset is reported in table 1. For comparison, the values for vessel number, area fraction, and vessel diameter previously reported by Wu and colleagues are shown to the right for days 3, 7, and 10 (7). In the samples analyzed, clear differences were appreciated between POD 7 and all other time points (figure 3). Vessel density was much greater at POD 7, and significantly greater at POD 10 than at POD 21. Fractal analysis showed a similar trend, with greater fractal dimension at POD 7 compared to all other time points (figure 3). The lacunarity measurements indicated that there was less empty space (or nonvascular tissue) at POD 7 compared to all other time points. Also, there was significantly less empty space at POD 10 compared to POD 21 (figure 3). (Importantly, figure 3 shows the lacunarity parameter, which is commonly reported as b and is *inversely* related to the actual lacunarity of the image.)

Next, the multifractal analysis of the images helped elucidate differences in the complexity of microvessels from groups at different time points and clearly illustrated the remodeling of the vessels at each time point (figure 4). In figure 4, the multifractal analysis is depicted as having a spectral output, where each curve represents the region of the multifractal spectra that is correlated to the multifractal behavior with a correlation coefficient of at least 0.95. The x axis represents the values of $\alpha(q)$ that were determined from our analysis, and the y axis represents the function $f(\alpha)$ at each given value of $\alpha(q)$. The resultant spectra are curves, where the right half of the curve describes the distribution of the empty space and the left half of the curve represents the distribution of the signal, or in this case, the microvascular staining. For each curve in figure 4, the plot indicates the mean value of each measured correlating point with respect to the postoperative day, and the error bars represent the 95% confidence interval for each mean.

In figure 4, vessels at POD 3 are illustrated by a dark blue curve to the left and below the other groups, which represents a vascular bed with a low fractal dimension (downward shift) and high lacunarity (leftward shift). At POD 7, the vessel morphology has shifted upward and to the right (red curve), indicating an increase in fractal geometry and a decrease in lacunarity, or nonvascular tissue, around the vessels within the fibrin interface. By POD 10, the spectra shifts back towards the left and downward (green curve); this indicates remodeling of the microvascular complexity, with decreasing fractal dimension and increasing lacunarity. Interestingly, at POD 14 (purple curve) the shift continues leftward and downward somewhat in equal proportion, but it does not deviate past the curve seen at POD 3, which indicates microvascular remodeling due to increasing nonvascular tissue and decreasing vessel complexity. By POD 21 (light blue curve), the spectrum has shifted further downward but in greater proportion towards the left. This is largely due to an increase in empty space (i.e., non-vascular tissue) around the vessels, without a significant decrease in the space occupied by the vessels.

The multifractal spectra were then analyzed for symmetry and heterogeneity, as previously described (8). The heterogeneity was plotted by comparing the moments, α (0), with the predicted moments, D (0), of a simple fractal (figure 5A). The predicted moments were shown to deviate from the 1:1, or perfectly symmetric, line, indicating that the images of the vessels and, thus, the distribution of the microvasculature were multifractal (i.e., there were differences in the complexity measures of capacity [D0], correlation [D1], and entropy [D2])

and also significantly heterogeneous. Finally, the multifractal spectra were analyzed for symmetry between the different time points. Given that the curves represent information about both the nonvascular and vascular spaces, the symmetry helps to describe with a statistical value the relative contributions and distributions of nonvascular and vascular tissue in the samples. In figure 5B at POD 3 and POD 7, there is clear separation of the spectra, with asymmetric features, as represented by the distance from the 1:1 line.

Discussion

The multifractal analysis was able to delineate the vessel morphologies at different time points and provided invaluable information about the space-filling qualities of the microvasculature in the fibrin interface. Also, the complete analysis of the multifractal spectra provided insight into the way the vessels filled the space at the different time points and how the vessels within the images contributed to the signal spectra.

Using the unique image processing method described herein, we were able to compare the vessel complexity in the fibrin interface of split-thickness skin grafts at days 3, 7, 10, 14, and 21 after graft implantation. In table 1, the new complexity measures (fractal dimension, multifractal dimension, and lacunarity) are compared to previous measures of vascularization (vessel area fraction, vessel count, vessel diameter) described by Wu and colleagues (7) and to the classical measure of vessel density (similar to area fraction), as described by Gould and colleagues (8). Interestingly, the results reported by Wu and colleagues for the area fraction correlate well with the values for density measured using the algorithm in this study (table 1). They demonstrate the development of new vasculature in the engrafted tissue, with an initial swelling of vessel density from POD 3 to POD 7, which may represent the early stages of vessel growth and invasion into the graft.

Vessel diameter was unchanged on average, but number fraction and area fraction increased from POD 3 to POD 7; this may represent a dramatic increase in density due to increasing numbers of vessels, with a symmetrical increase in larger and smaller vessels. At this point, classical methods of vascular morphology report means of vessel diameters but cannot determine whether the increasing vessel density is from increased proportions of very large (30 microns) or very small (2–3 microns) vessels or vessel elements. It is apparent when examining histograms of vessel diameters that the growth of a single large-diameter vessel can skew the mean vessel diameter measurement dramatically. The ratio of vessel mean to vessel density within a sample is used as a surrogate for vessel network complexity, *but in fact, this ratio does not define the complexity of microvessel networks* because of these statistically powerful variations.

In this study, multifractal analysis helped to demystify the remodeling process, and it suggests that the actual complexity of the split-thickness skin graft network measured as the simple fractal dimension (D0) increases dramatically, from 1.56 at POD 3 to 1.77 at POD 7. This confirms an increase in not only similar-diameter vessels but also network complexity, and as the network remodels and the vessel density decreases from POD 7 to POD 10, there is a decrease in the network complexity. The density decrease from POD 7 to POD 10 may represent the vessel pruning that occurs as new vessels outgrow their usefulness and overshoot the demands of the engrafted tissues. Interestingly, in the grafts examined on days 14 and 21, the density seemed to slowly decrease, from 0.12 on POD 10 to 0.09 and then 0.06, which represents a 25% and then 33% decrease in density.

In tandem, complexity measures help to parse out the nature of the decreasing density. Lacunarity analysis showed no difference in the complexity of the surrounding non-vascular tissues from POD 14 (0.51) to POD 21 (0.51). However, there was a significant decrease in

the fractal dimension (D0) of the vessels (from 1.62 to 1.57), which represents a decrease in vessel complexity. This is *one of the first studies* to show that the decrease in density is actually due to a characteristic change in vessel network complexity and not simply a decrease in vessel area proportion. Also, the multifractal analysis showed that not only did the fractal dimension and the vessel network complexity decrease from POD 14 to POD 21 but also the decrease was more dramatic in the correlation dimension (D1) and the entropy dimension (D2). This indicates increasing differences in the spatial distribution of vessels and decreasing entropy of the system, which may reflect the pruning of nondescript small vessels of growth and invasion and their replacement with vessels ideal for distribution and metabolic exchange in an orderly fashion. Although this is only a postulation, these extra parameters of microvessel morphological complexity provide more information into the system and in the future may lead to high-throughput methods for comparing vessel remodeling and physiological microvascular changes in similar systems.

As the multifractal spectra representative of microvessel complexity moved upward with respect to the Y axis, they indicated increasing fractal dimension or microvessel complexity. And as the curves moved from right to left, they indicated a greater contribution of the nonvascular space around the vessels to the overall image. In this manner, the multifractal analysis helped to differentiate statistically the microvascular remodeling states by combining information about the microvascular complexity and lacunarity into one graph and, thus, encapsulating the microvascular remodeling process. Although it was hard to statistically compare the POD 3 time point to the POD 10, 14, and 21 time points using the single value of vessel density, it was possible, using this spectral analysis, to show that the later time points had vessel networks that are somewhere between the POD 3 and POD 7 values. This observation highlights the usefulness of the multifractal spectral analysis technique.

Symmetry and heterogeneity analyses provided insight about the space-filling properties of the vessel beds being measured and a unique, statistically separate signal or *'fingerprint'* for each measured microvasculature. Heterogeneity analysis showed deviation from the one to one line, which reinforced the fact that multifractal analysis was appropriate for the characterization of the microvascular complexity. With respect to the symmetry findings, interestingly, at POD 10, the spectra appear to be closely symmetric, and then at POD 14 and POD 21, the symmetry is lost again. This may mean that early on there is a better balance between the vascular complexity and the complexity of the surrounding avascular space (tissue space). Over time the symmetry is lost and shifts towards the region below the line indicating a greater contribution of complexity to the spectra of the avascular regions of the images (or the tissues) and then this shift is corrected at 21 days as the symmetry moves back to above the 1:1 line, indicating at this time point the main contributor to the multifractal spectrum comes from the vessel components. One may theorize that this reflects a shift in remodeling where the vessels are pruning at 14 days, and thus they are less complex than the surrounding avascular tissues, and that there is a flux to a more complex state by 21 days, but this remains to be proven or demonstrated elsewhere. Future studies may help to determine the relevance of these findings and effects.

In previous studies, Wu and colleagues looked at the vessel diameter, area fraction and volume fraction, and thus reported scale dependent measures of microvascular morphology (7). Many other studies have reported similarly the vessel density or the vessel diameters measured in native tissues (32), pathological tissues in cancer (33,34) or ischemic disease (35), and in tissue engineered constructs (36). Only recently has this novel technology been developed to analyze the vessel morphology in a scale invariant manner, using fractal, lacunarity and multifractal analysis, in developmental studies (8,12), and in applications in tissue engineering (37), novel biomaterials (38,39) and cancer vessel biology (16,20). The

application of fractal theory to biological systems has proven monumental to new understanding of how simple rules and parameters for growth can create complex systems (28,40,41) and organisms (10), and undoubtedly this area will provide greater insight into vessel biology and angiogenesis.

In previous publication by Gould et al. it was demonstrated that the fractal values can be preserved in each stack image, though this is a surrogate for true three dimensional analyses. This method could be extended to a true three dimensional multifractal analysis if the data set were transposed to voxels instead of pixels, and thus true three dimensional analysis could be undertaken. However this approach may take greater computational power and time, and may not significantly alter approximations of complexity in thin microvascularized tissues, or in the context of the microvasculature. Rather it may make a bigger difference in examination of distributory networks like larger vessels in the body.

This study has provided new scale-invariant measures of the microvascular morphology found in the interface between the donor skin graft tissue and the recipient site. Hopefully the parameters provided here will help to inform the process of grafting and future studies of microvascular engraftment and anastamosis where optimization is desired. These parameters of microvessel morphological complexity may help to provide more information about engraftment, and may help to provide high throughput methods for comparing vessel remodeling and physiological microvascular changes in similar systems. The scale-invariant parameters described and utilized here are rapidly demonstrating utility in the study of microvascular morphology (8,12,22,35,42,43), and this study adds to the evidence suggesting that multifractal analysis and other scale-invariant tools may provide acceptable design constraints for engineered systems (10,44–46) Ideally, large-scale implementation of this kind of quantification scheme could help to parse out differences between vessel groups when simple and more common quantification methods, like branching and vessel diameters, cannot. These new methods provide an additional measurement apparatus when comparing experiments applied on different scales or using more classical or more subjective quantification schemes. Importantly, we have now determined the scale-invariant space-filling parameters associated with these physiological events in graft/recipient development. In the future, we hope to use these design parameters to advance the field of tissue engineering by examining other microvascular morphologic characteristics in transplanted materials and fine-tuning biomaterial scaffolds to mimic normal tissue microvasculature for grafting purposes.

Perspectives

Here we have shown that these scale invariant parameters provide complementary information to classical measures, and are practical in that they are measured with automated tools, as opposed to classical methods which require hand counting and measurements. The functional characteristics of the microvasculature (including capillaries which are not fractal) are physiologically and clinically relevant. These complexity measures may in the future be connected to functional properties, including oxygen delivery and developmental angiogenesis. This study helps to inform the microvascular community about a new growing technological method (based on relatively recent breakthroughs in math and physics from the 1960s (13) and even more recent breakthroughs in computational algorithms and image analysis techniques (8)) as well as supplying evidence of the utility of this analysis in classifying complex vessel beds with similar or overlapping density or diameter, as well as the non vascular tissues surrounding microvascular networks. These morphological tools may also provide unique insight into the critical steps in vessel remodeling, changing the way that pruning and microvascular maturation is described and encapsulating the critical development of vessel network complexity during these stages.

Acknowledgments

DG prepared images for analysis, collected and analyzed data, formulated figures, and wrote the manuscript. GR supervised experiments, collected images of the tissues, and provided editorial feedback on the preparation of the manuscript. DG would like to acknowledge the American Heart Association predoctoral fellowship 10PRE4190021, the Baylor College of Medicine Medical Scientist Training Program, and the C Thomas Caskey MD PhD training fellowship. DG would like to acknowledge Mary Dickinson, PhD. and Tegy Vadakkan, PhD., previous mentors who assisted in the development of the algorithm (which is available online, free at the Matlab central file sharing database) applied in this study, this algorithm was developed during DG's doctoral thesis prior to this study and is reported in Gould et al. (8). The authors would also like to acknowledge Xuemei Wu and Charles Patrick for their contribution of the study detailed in the reference list. Importantly, the authors would like to acknowledge the input of Dawn Chalaire as editorial staff at MDACC. This study was funded in part by grants from The University of Texas MD Anderson Cancer Center (number 80094186), the Plastic Surgery Education Foundation (number 01-99-00141), and the National Institutes of Health (HL 062341) and a generous gift from the Maurice Amado Foundation.

Abbreviations

STSG	Split thickness skin graft
D(0)	Fractal dimension
D(1)	Correlation dimension
D(2)	entropy dimension

References

1. Cannon B. Plastic Surgery. New England Journal of Medicine. 1948; 239:435–442. [PubMed: 18881641]
2. Orgill DP. Excision and Skin Grafting of Thermal Burns. New England Journal of Medicine. 2009; 360:893–901. [PubMed: 19246361]
3. Lemaître G, Nissan X, Baldeschi C, Peschanski M. Concise Review: Epidermal Grafting: The Case for Pluripotent Stem Cells. STEM CELLS. 29:895. [PubMed: 21472820]
4. Kempf M, Miyamura Y, Liu P-Y. A denatured collagen microfiber scaffold seeded with human fibroblasts and keratinocytes for skin grafting. Biomaterials. 32:4782. [PubMed: 21477857]
5. Shaterian A, Borboa A, Sawada R, et al. Real-time analysis of the kinetics of angiogenesis and vascular permeability in an animal model of wound healing. Burns. 2009; 35:811. [PubMed: 19423227]
6. Brey EM, King TW, Johnston C. A Technique for Quantitative Three-Dimensional Analysis of Microvascular Structure. Microvascular Research. 2002; 63:279. [PubMed: 11969305]
7. Wu X, Kathuria N, Patrick CW, Reece GP. Quantitative analysis of the microvasculature growing in the fibrin interface between a skin graft and the recipient site. Microvascular Research. 2008; 75:119. [PubMed: 17631360]
8. Gould DJ, Vadakkan TJ, Poche RA, Dickinson ME. Multifractal and lacunarity analysis of microvascular morphology and remodeling. Microcirculation. 2011; 18:136–151. [PubMed: 21166933]
9. Moisy F. Boxcount. MATLAB Central. 2006
10. Mandelbrot, BB. The Fractal Geometry of Nature. 20th ed.. New York: Freeman; 1982.
11. Mancardi D, Varetto G, Bucci E, et al. Fractal parameters and vascular networks: facts & artifacts. Theoretical Biology and Medical Modelling. 2008; 5:12. [PubMed: 18637183]
12. Stosic; Tatijana; Stosic; Borko, D. Multifractal analysis of human retinal vessels. New York, NY, USA: Institute of Electrical and Electronics Engineers; 2006.
13. Mandelbrot B. How long is the coast of britain? statistical self-similarity and fractional dimension. Science. 1967; 156:636–638. [PubMed: 17837158]
14. Tolle CR, McJunkin TR, Gorsich DJ. An efficient implementation of the gliding box lacunarity algorithm. Physica D: Nonlinear Phenomena. 2008; 237:306.

15. Posadas AND, Gimenez D, Quiroz R, Protz R. Multifractal Characterization of Soil Pore Systems. Soil Sci Soc Am J. 2003; 67:1361–1369.
16. Baish JW, Jain RK. Fractals and Cancer. Cancer Res. 2000; 60:3683–3688. [PubMed: 10919633]
17. Lopes R, Betrouni N. Fractal and multifractal analysis: A review. Medical Image Analysis. 2009; 13:634. [PubMed: 19535282]
18. LIEW G. The Retinal Vasculature as a Fractal: Methodology, Reliability, and Relationship to Blood Pressure. Opthalmology. 2008; 115:1951–1956.
19. Landini G, Murray PI, Misson GP. Local connected fractal dimensions and lacunarity analyses of 60 degrees fluorescein angiograms. Invest. Ophthalmol. Vis. Sci. 1995; 36:2749–2755. [PubMed: 7499097]
20. Jain RK, Munn LL, Fukumura D. Dissecting tumour pathophysiology using intravital microscopy. Nat Rev Cancer. 2002; 2:266. [PubMed: 12001988]
21. Jain RK. Normalization of tumor vasculature: an emerging concept in antiangiogenic therapy. Science. 2005; 307:58–62. [PubMed: 15637262]
22. Guidolin D, Vacca A, Nussdorfer GG, Ribatti D. A new image analysis method based on topological and fractal parameters to evaluate the angiostatic activity of docetaxel by using the Matrigel assay in vitro. Microvascular Research. 2004; 67:117. [PubMed: 15020202]
23. Jain RK, Schlenger K, Hockel M, Yuan F. Quantitative angiogenesis assays: Progress and problems. Nat Med. 1997; 3:1203. [PubMed: 9359693]
24. Rasband, W. Image J plugin: NIH. 2010.
25. Vadakkan T. Multifractal spectrum of a binary image. MATLAB Central. 2009
26. Vadakkan T. Lacunarity of a binary image. MATLAB Central. 2009
27. Posadas A, Gimenez D, Quiroz R, Protz R. Multifractal characterization of soil pore systems. Soil Science Society Of America Journal. 2003; 67:1361–1369.
28. Meneveau C, Sreenivasan KR. The multifractal nature of turbulent energy dissipation. Journal of Fluid Mechanics Digital Archive. 1991; 224:429.
29. Frisch U, Vergassola M. A Prediction of the Multifractal Model: the Intermediate Dissipation Range. EPL (Europhysics Letters). 1991; 14:439.
30. Chhabra AB, Jensen RV. Direct determination of the f(a) singularity spectrum. Phys. Rev. Lett. 1989; 62:1327–1330. 1989. [PubMed: 10039645]
31. Zaia A, Eleonori R, Maponi P, et al. MR Imaging and Osteoporosis: Fractal Lacunarity Analysis of Trabecular Bone. Information Technology in Biomedicine, IEEE Transactions on. 2006; 10:484.
32. Miyawaki T, Matsui K, Takashima S. Developmental characteristics of vessel density in the human fetal and infant brains. Early Human Development. 1998; 53:65. [PubMed: 10193927]
33. Sabo E, Boltenko A, Sova Y, et al. Microscopic Analysis and Significance of Vascular Architectural Complexity in Renal Cell Carcinoma. Clinical Cancer Research. 2001; 7:533–537. [PubMed: 11297244]
34. Holash J, Maisonpierre PC, Compton D, et al. Vessel Cooption, Regression, and Growth in Tumors Mediated by Angiopoietins and VEGF. Science. 1999; 284:1994–1998. [PubMed: 10373119]
35. Doubal FN, MacGillivray TJ, Patton N, et al. Fractal analysis of retinal vessels suggests that a distinct vasculopathy causes lacunar stroke. Neurology. 2010; 74:1102–1107. [PubMed: 20368631]
36. Richardson TP, Peters MC, Ennett AB, Mooney DJ. Polymeric system for dual growth factor delivery. Nat Biotech. 2001; 19:1029.
37. Saik JE, Gould DJ, Watkins EM, et al. Covalently immobilized platelet-derived growth factor-BB promotes angiogenesis in biomimetic poly(ethylene glycol) hydrogels. Acta Biomater. 2011; 7:133–143. [PubMed: 20801242]
38. Leslie-Barbick JE, Saik JE, Gould DJ, et al. The promotion of microvasculature formation in poly(ethylene glycol) diacrylate hydrogels by an immobilized VEGF-mimetic peptide. Biomaterials. 32:5782. [PubMed: 21612821]
39. Saik JE, Gould DJ, Keswani AH, et al. Biomimetic Hydrogels with Immobilized EphrinA1 for Therapeutic Angiogenesis. Biomacromolecules. 12:2715. [PubMed: 21639150]

40. Lam, NSN.; De Cola; Lee. Fractals in Geography. Englewood Cliffs, N.J: Prentice Hall; 1993.
41. Wolf M. Multifractility of snowflakes. Fractals. 1996; 4:477–493.
42. Avakian A, Kalina RE, Helene Sage E, et al. Fractal analysis of region-based vascular change in the normal and non-proliferative diabetic retina. Current Eye Research. 2002; 24:274–280. [PubMed: 12324866]
43. Grauslund J, Green A, Kawasaki R, et al. Retinal Vascular Fractals and Microvascular and Macrovascular Complications in Type 1 Diabetes. Ophthalmology. 2010 In Press, Corrected Proof.
44. Weibel ER. Fractal geometry: a design principle for living organisms. American Journal of Physiology - Lung Cellular and Molecular Physiology. 1991; 261:L361–L369.
45. JB Bassingthwaighte, LSL.; West, BJ. Fractal Physiology. New York, NY: Oxford University; 1994.
46. Jaan, K. On the fractality of the biological tree-like structures. Hindawi Publishing Corporation; 1998.

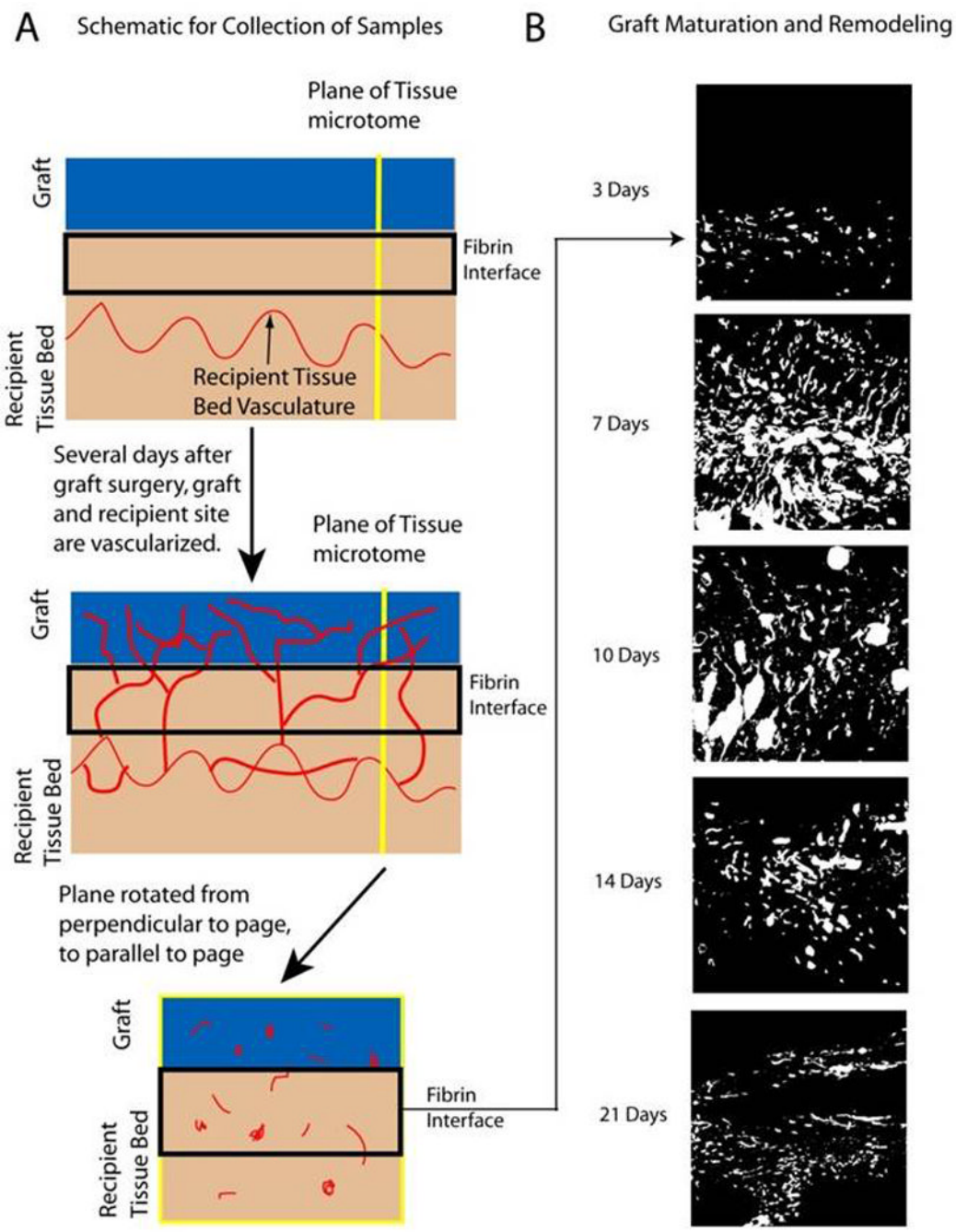

Figure 1.

Graft/recipient interface and tissue sectioning. Panel A illustrates how the graft was surgically fixed to the recipient site. After allowing time for engraftment, the graft was harvested with the underlying muscle from the recipient site, and the tissue was sectioned in a perpendicular fashion to allow for the visualization of the fibrin interface between the graft and the recipient site. Blood vessels in the interface were stained with CD 31 antibodies, imaged, and thresholded to provide raw images as seen in panel B. Panel B highlights the study's general trend, with more vessels seen at POD 7 and then remodeling over the following 14 days as vessels organized throughout the interface.

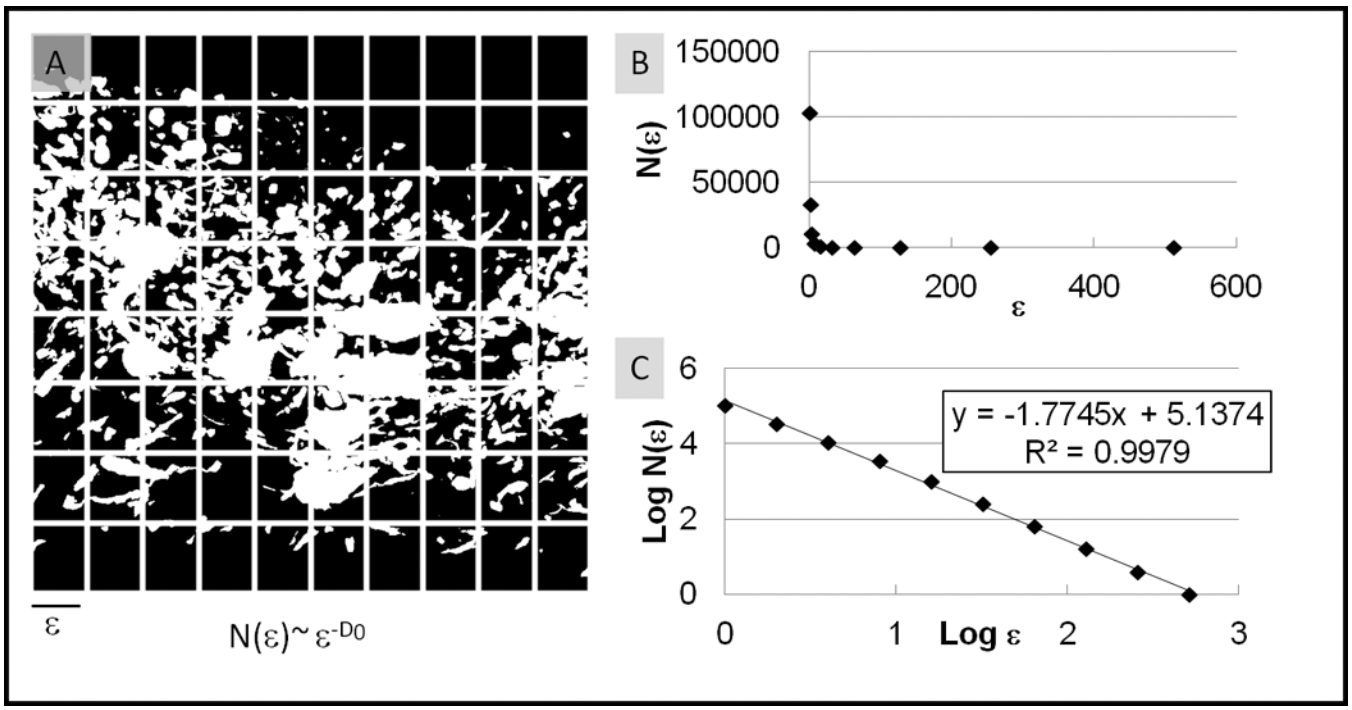

Figure 2.

The box-counting algorithm. This figure highlights the process of determining the simple fractal dimension (D0) from an image of blood vessels. The box side length is set by overlaying a grid on the image (A), and then the number of positive boxes is plotted versus the box side length (B). The log-log plot of B yields a linear relationship (C) in which the slope of the line represents the relationship between side length and scale of the box; this relationship is the fractal dimension.

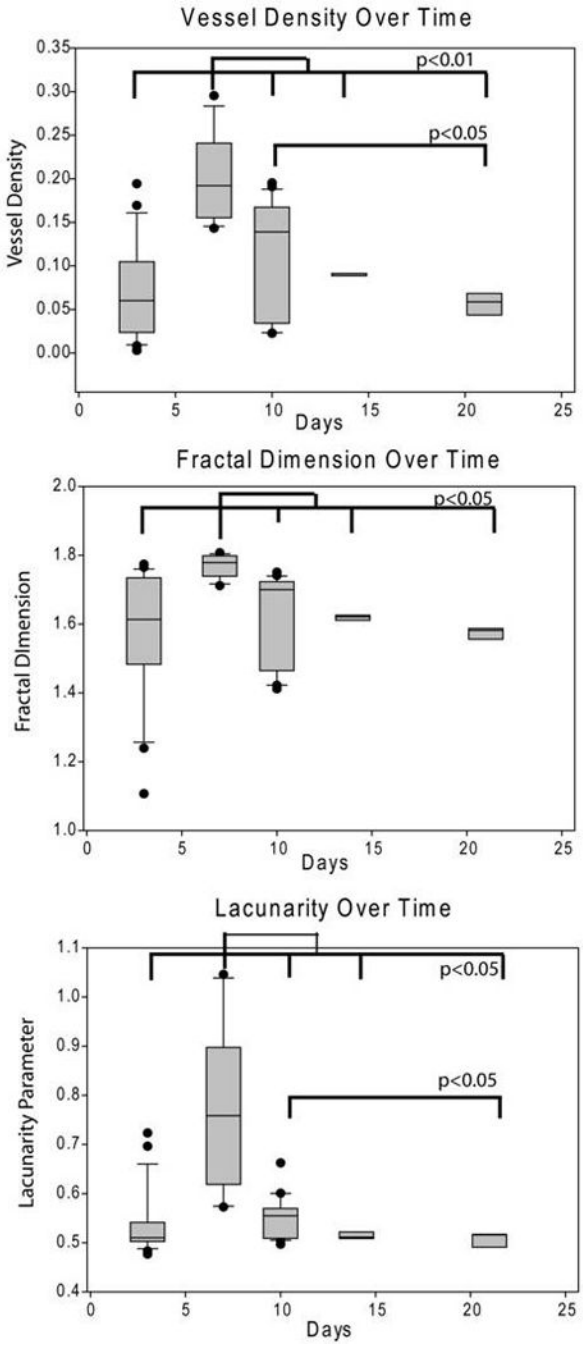

Figure 3.

Scale-invariant parameters to classify vessel morphology. Figure 3 demonstrates box plots of the various values of the measured parameters from the different groups. Clearly, in all three measures--density, fractal dimension, and lacunarity--there are significant differences between the POD 7 time point and all others. Also, in the lacunarity and vessel density groups, there are significant differences between the POD 10 and the POD 21 time points. These trends help to graphically show the relative increase in vessel density and network complexity (fractal dimension increase and decrease of distribution of empty space as seen by increase in lacunarity parameter) from POD 3 to POD 7. Also, they show the opposite

trend from POD 7 to POD 21, which is indicative of a remodeling event, where the vessels regress after initial growth to provide only the necessary perfusion to the engrafted skin.

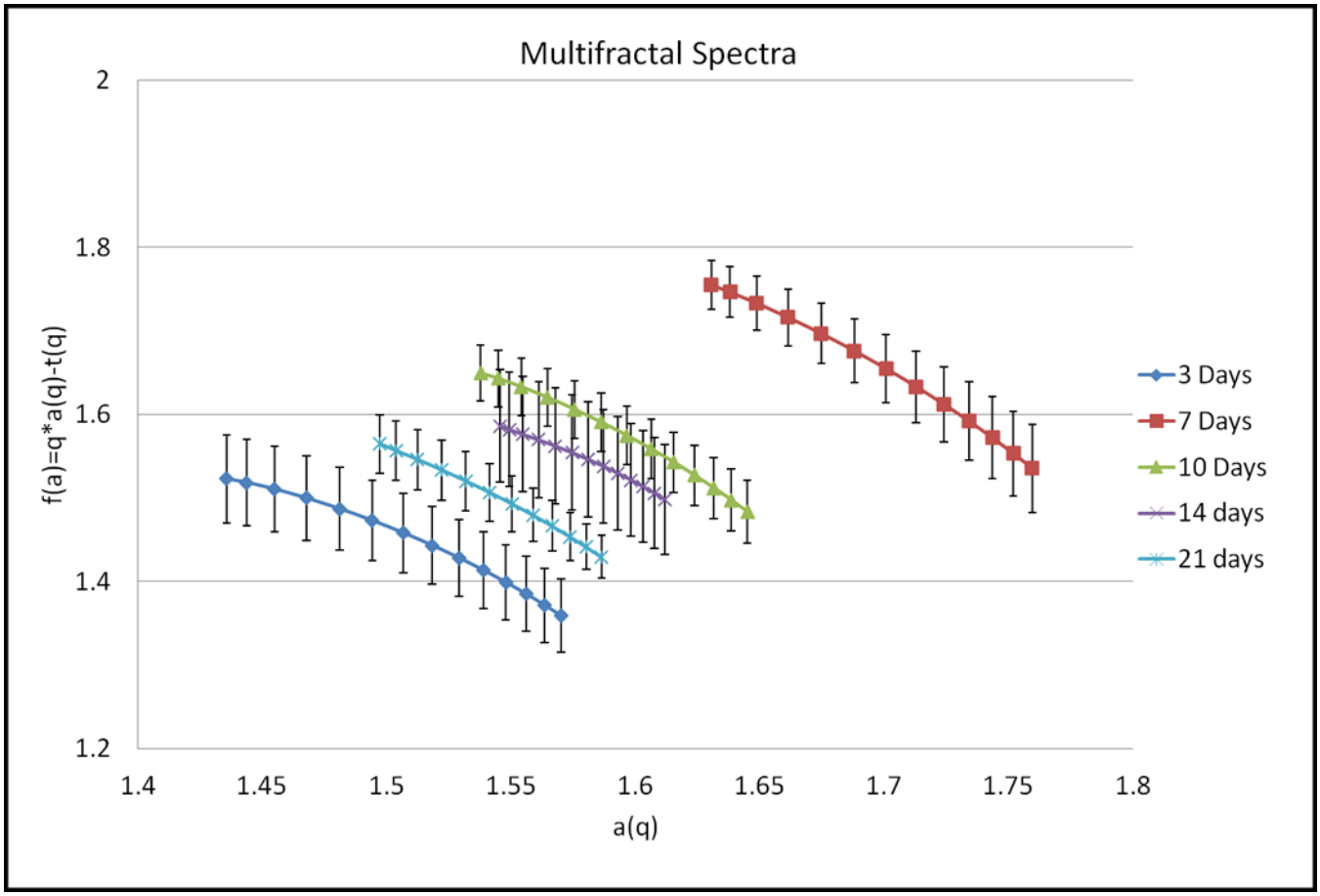

Figure 4.
Multifractal analysis of the skin grafts. Figure 4 demonstrates a multifractal spectrum for each time point examined in the study. Importantly, there is good statistical separation between the time points at POD 3, 7, 10, 14, and 21. As these curves move upward with respect to the y axis, the fractal dimension, or microvascular complexity, increases. As the curves move from right to left on the X axis, the avascular space surrounding the vessels increases. In this manner, the multifractal analysis statistically differentiates the remodeling states by combining information about complexity and lacunarity into one graph.

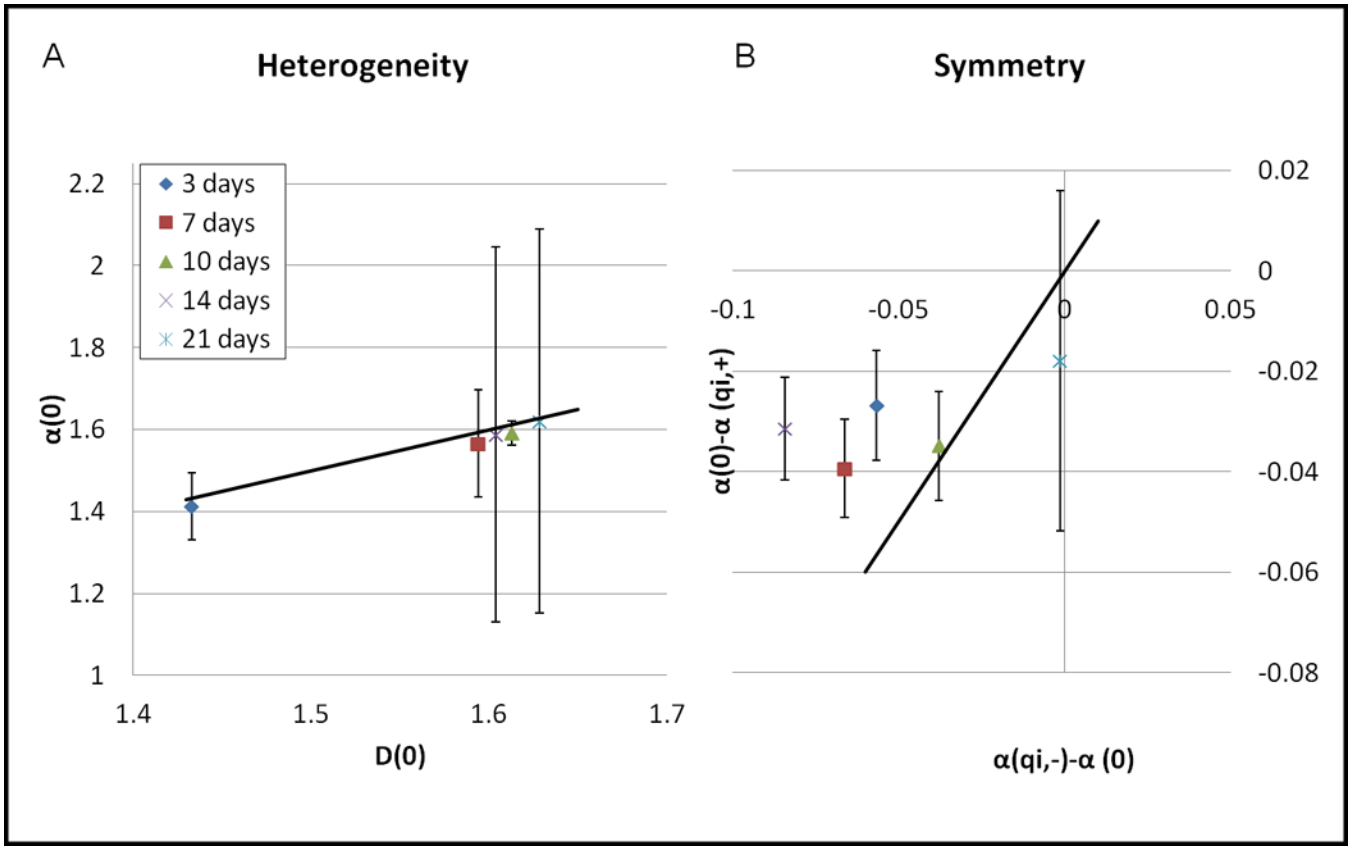

Figure 5.

Heterogeneity and symmetry. Figure 5 examines the heterogeneity and symmetry of the multifractal spectra at each time point. The heterogeneity curve (A) shows all points below the 1:1 homogeneity line, graphically demonstrating the heterogeneous distribution of the spectra (supporting the use of multifractal analysis in classifying these vessel networks). In the symmetry analysis, there are differences in the contributions of the vessels and the surrounding supportive tissue at POD 3, 7, and 14, where the vessels themselves contribute greatly to the overall network in the images. The POD 10 time point represents a moment where the contributions of empty space and vessels are relatively evenly distributed. At POD 21, there is a greater contribution of the other tissues or unlabeled spaces around the microvessels to the overall network complexity.

Table 1

Morphological Parameters of Skin Graft Microvessels. Table 1 displays all the pertinent scale-invariant factors that, as a group, help to define the vascular morphology seen in the fibrin interface. Clear differences are seen over time between several factors. The most obvious difference is between the POD 7 time point for all measures and the other time points ($p < 0.01$ for all comparisons). The generalized fractal dimensions are representative of the simple fractal dimension (D0), the correlation dimension (D1), and the entropy dimension (D2). These are all representative of the fractal behavior of other features of the vessel images, or mathematically, of the point values at different moments in the spectra.

Days	Vessel Density	Fractal Dimension	Generalized Fractal Dimension			Lacunarity Parameter	Number	Area Fraction † (mm^2)	Vessel Diameter † (μM)
			D0	D1	D2		(vessel/mm		
3	0.07 ± 0.05	1.56 ± 0.18	1.55 ± .019	1.56 ± 0.18	1.56 ± 0.18	0.54 ± 0.06	116	0.009	10.25
7	0.20 ± 0.05	1.77 ± 0.03	1.76 ± 0.03	1.78 ± 0.03	1.78 ± 0.04	0.77 ± 0.17	291	0.021	10.89
10	0.12 ± 0.09	1.63 ± 0.13	1.61 ± 0.15	1.63 ± 0.15	1.64 ± 0.15	0.74 ± 0.88	148	0.012	10.56
14	0.09 ± 0.00	1.62 ± 0.01	1.60 ± 0.01	1.62 ± 0.01	1.63 ± 0.01	0.51 ± 0.01			
21	0.06 ± 0.01	1.57 ± 0.02	1.57 ± 0.02	1.57 ± 0.02	1.57 ± 0.03	0.51 ± 0.01			

The recorded values from Wu et al. (7) for vessel number fraction (vessels/mm^2), area fraction (mm^2), and vessel diameter (μm) are reported here with permission and are demoted with †. They highlight the classical measures of morphology and show there are measureable changes in number fraction and area fraction from POD 3 to POD 10, as the vessel diameters on average do not change. This may indicate increasing complexity early on due to increasing total vessel number, whereas later decreases in complexity, as highlighted by the multifractal analysis, may come from changes in the complexity of the vessel beds, with less of a decrease in complexity of the vessels and no change in the surrounding nonvascular tissues but rather changes in the vessel networks and distributions of vessels.